

# Three-Dimensional Nanopillar Arrays-Based Efficient and Flexible Perovskite Solar Cells with Enhanced Stability

Yiyi Zhu, Lei Shu, Swapnadeep Poddar, Qianpeng Zhang, Zhesi Chen, Yucheng Ding, Zhenghao Long, Suman Ma, Beitao Ren, Xiao Qiu, and Zhiyong Fan\*



Cite This: *Nano Lett.* 2022, 22, 9586–9595



Read Online

ACCESS |

Metrics & More



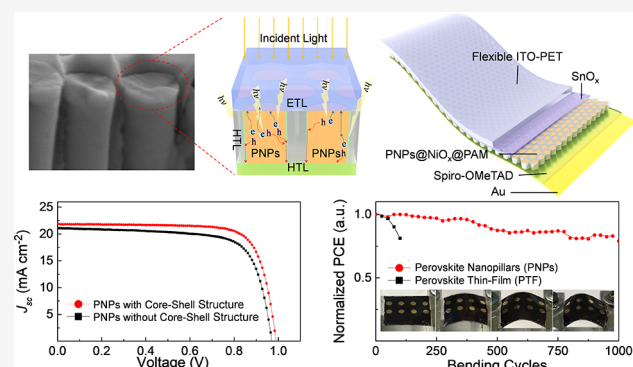
Article Recommendations



Supporting Information

**ABSTRACT:** Perovskite nanopillars (PNPs) are propitious candidates for solar irradiation harvesting and are potential alternatives to thin films in flexible photovoltaics. To realize efficient daily energy output, photovoltaics must absorb sunlight over a broad range of incident angles and wavelengths congruent with the solar spectrum. Herein, we report highly periodic three-dimensional (3D) PNP-based flexible photovoltaics possessing a core–shell structure. The vertically aligned PNP arrays demonstrate up to 95.70% and 75.10% absorption at peak and under an incident angle of 60°. The efficient absorption and the orthogonal carrier collection facilitate an external quantum efficiency of 84.0%–89.18% for broadband wavelength. PNPs have been successfully implemented in flexible solar cells. The porous alumina membrane protects PNPs against water and oxygen intrusion and thereby imparts robustness to photovoltaic devices. Meanwhile, the excellent tolerance to mechanical stress/strain enables our unique PNP-based device to provide efficient solar-to-electricity conversion while undergoing mechanical bending.

**KEYWORDS:** Perovskite, Solar Cell, Nanowires, Flexible Devices



Flexible solar cells have enormous significance in the genre of photovoltaic technologies because of their lower payback time, light weight, and pliability. They are receiving heightened attention for the energy supply for wearable and portable devices and building-integrated applications.<sup>1–3</sup> Conventionally, flexible thin-film photovoltaics degrade during repetitive mechanical bending.<sup>4–7</sup> Reducing thickness is a general strategy to improve mechanical robustness, whereas this will suppress light-harvesting capability.<sup>8,9</sup> In this regard, designing and fabricating nanostructured devices open a new path to addressing this issue,<sup>6,10–12</sup> since prior reports have proven that the nanoscale geometry is beneficial to facilitate strain relaxation, defect tolerance, etc.<sup>7,13–19</sup>

Hitherto, many works have explored semiconducting nanopillars for flexible photovoltaics,<sup>10,11,20</sup> for instance, silicon,<sup>21</sup> polymer blend,<sup>22,23</sup> dye-sensitized nanopillars,<sup>24</sup> CdS,<sup>11</sup> etc. Nanopillars offer guiding channels for propagating carriers and photons along the pillars. The efficient carrier transport and intensive light trapping render nanopillar-based devices with unique features, such as fast response for photodetectors and attractive angular behavior for photovoltaics.<sup>10,11,15,20,25–31</sup> Another critical advancement is the radial built-in electric field.<sup>32–35</sup> The heterojunction interface at the nanoscale allows efficient carrier extraction.<sup>11,15,20,25</sup> In this manner, the photogenerated carriers only need to traverse

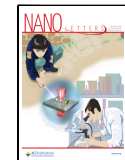
a short path and reach the boundary of p–n junctions, decreasing the chances of volumetric recombination.<sup>36</sup> Nevertheless, the large contribution from the surface renders optoelectronic properties to be significantly impacted by the surface features.<sup>10</sup>

Recently, organic–inorganic halide perovskite solar cells (PSCs) emerged as promising candidates for nanoengineered photovoltaics.<sup>37–39</sup> These perovskite materials exhibit desirable optical-electrical properties, such as high defect tolerance, long diffusion length, strong absorption, etc. In particular, the high defect tolerance, which originates from defects with low formation energy only creating shallow defect states, makes the elimination of surface defects less crucial for perovskites when compared to a broad array of other materials.<sup>37,40</sup> This feature enables nano- or even quantum-engineered perovskites based on light-emitting diodes (LEDs), high-emission photovoltaics, and high open-circuit voltage ( $V_{oc}$ ) even without the core–shell structure.<sup>6,37,41,42</sup>

Received: September 22, 2022

Revised: November 9, 2022

Published: November 17, 2022



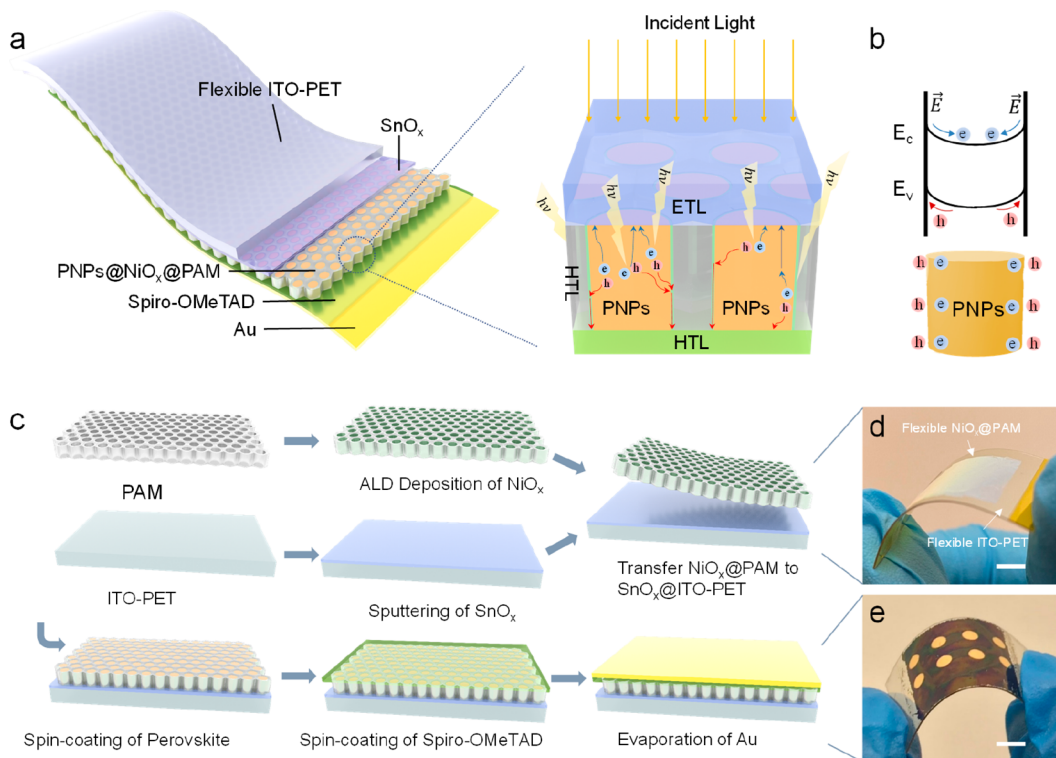


**Figure 1. Device structure, photograph, and fabrication procedure of 3D PNPs arrays-based device.** (a) Complete structure diagram and the cross-sectional schematic diagram of PNP-based solar cells. (b) The schematic band structure of the PNPs crystal surface, where the built-in electric field is formed due to the p-type doping of PNPs crystal surface regions, in which thickness is 1 nm, with a doping level of  $10^{15} \text{ cm}^{-3}$  at an energy level of 0.1 eV above the valence band minimum (VBM).<sup>37,49,50</sup> (c) Schematic illustration of the fabrication procedure for PNP-based devices. Photographs of (d)  $\text{NiO}_x$ -coated PAM ( $\text{NiO}_x$ @PAM) implemented on the  $\text{SnO}_2$  coated ITO-PET ( $\text{SnO}_2$ @ITO-PET) and (e) complete device, scale bars 1 cm.

To date, the growth of high-quality perovskite nanopillars (PNPs) with well-defined geometry has rarely been reported. In fact, the development of nanophotovoltaics is rather difficult and lacks controllability and precision.<sup>43,44</sup> Herein, we report a strategy to controllably construct highly periodic three-dimensional (3D) PNP arrays for flexible photovoltaics with radial junctions. The effective light-trapping inside PNPs combined with orthogonal carrier collection results in 84.0%–89.18% EQE over a broad range of wavelengths and improved short-circuit current density ( $J_{sc}$ ) over a wide range of incidence angles. Another attractive feature of our PNP-based device is its excellent mechanical stress/strain tolerance. Confirmed by simulation and experiment, PNPs exhibit an outstanding ability for strain relaxation, along with strong adhesion to the substrate. Moreover, benefiting from the self-encapsulation of porous alumina membrane (PAM), a PNP-based device exhibits excellent long-term stability and remarkable photostability.

Figure 1a is the schematic of the PNP-based solar cell device. One advantage of our strategy is the freedom of material design in the perovskite composition. Herein,  $\text{Cs}_{0.05}\text{FA}_{0.83}\text{MA}_{0.12}\text{PbBr}_{0.33}\text{I}_{2.67}$  is used, a mixed cation and halogen-based perovskite with high tolerance against moisture and oxygen.<sup>45</sup> Figure 1a schematically shows the orthogonal collection and separation of photogenerated excitons into free carriers.<sup>10,11,37,46</sup> The device comprises vertically aligned arrays of radial junctions surrounding PNPs, with indium-doped tin oxide (ITO) and Au as the contact electrodes. Particularly, p-type  $\text{NiO}_x$  and 2,2',7,7'-tetrakis[N,N-di(4-methoxyphenyl)-amino]-9,9'-spirobifluorene (spiro-OMeTAD) serve as the

hole transport layers (HTLs), and  $\text{SnO}_2$  acts as the electron transport layer (ETL). The flexible solar cell is fabricated on a transparent poly(ethylene terephthalate) (PET) substrate to ensure pliability.

The high-performance cells rely on efficiently collecting photogenerated carriers before their recombination.<sup>37</sup> Recent studies found that the electron mobility in perovskite is dominant over the hole.<sup>47,48</sup> Besides, photogenerated holes of perovskite tend to accumulate on its crystal surfaces and generate hole currents (Figure 1b).<sup>49,50</sup> This is based on the assumption that uncoordinated ions at the perovskite crystal surface cause the p-type doping crystal surface and yield band bending. The band bending that occurs close to the PNPs crystal surface will improve the separation of electron–hole owing to the built-in electric field in this region.<sup>37,49–51</sup>

It is of importance to enhance the hole collection in the PNP-based PSCs. Herein, each PNP is wrapped around  $\text{NiO}_x$ , forming a core–shell structure. The wrap-around junctions significantly increase the interfacial areas between the PNPs and HTL, allowing holes to transit through a short path to reach the collection junction. Apart from that, the shell layer  $\text{NiO}_x$  has much higher carrier mobilities ( $\mu_h = 4.4\text{--}5.2 \text{ cm}^2 \text{ V}^{-1} \text{ s}^{-1}$ )<sup>52,53</sup> than spiro-MeOTAD ( $\mu_h = 10^{-4} \text{ cm}^2 \text{ V}^{-1} \text{ s}^{-1}$ ).<sup>49</sup> Thus,  $\text{NiO}_x$  can efficiently conduct holes from the perovskites' crystal surface to spiro-MeOTAD. More discussion about the heterostructure design can be found in Figures S1 & S2.

The fabrication process of PNPs (Figure 1c) uses PAM as the template for achieving highly regular PNP arrays. Briefly,  $\text{SnO}_2$  is sputtered on top of a clean ITO-PET substrate. PAM is fabricated by low-cost electrochemical anodization of

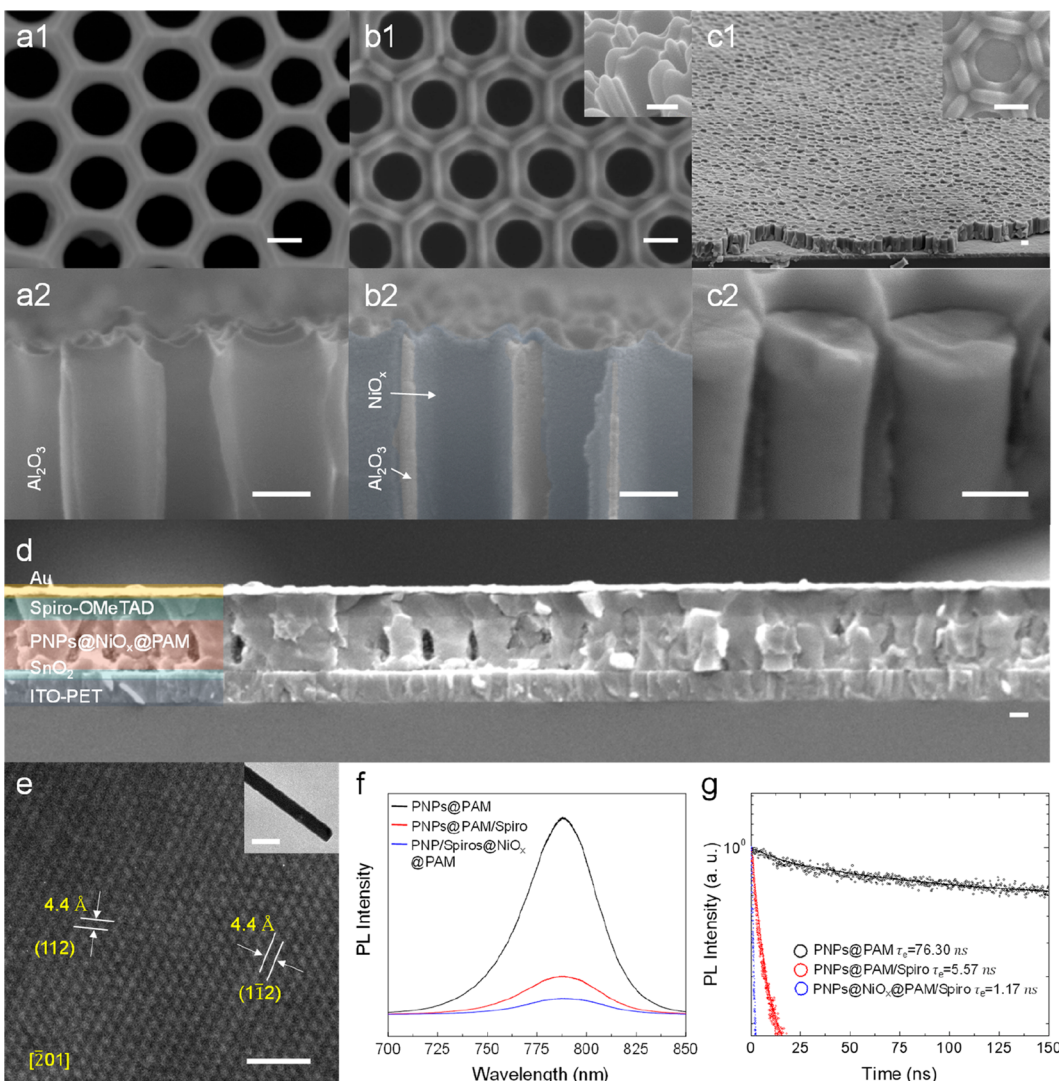


**Figure 2. The morphology and improved carrier collection of 3D  $\text{Cs}_{0.05}\text{FA}_{0.83}\text{MA}_{0.12}\text{PbBr}_{0.33}\text{I}_{2.67}$  PNPs device.** The top-view and cross-sectional SEM images of (a1, a2) PAM, (b1, b2)  $\text{NiO}_x$ @PAM. (inset) Tilted-angle view, scale bars 200 nm. Tilted-angle view of (c1, c2) PNPs encapsulated in  $\text{NiO}_x$ @PAM (PNPs@ $\text{NiO}_x$ @PAM). (inset) Top view, scale bars 200 nm. (d) Cross-sectional SEM image of the whole device based on PNPs@ $\text{NiO}_x$ @PAM, scale bars 200 nm. (e) HRTEM view of  $\text{Cs}_{0.05}\text{FA}_{0.83}\text{MA}_{0.12}\text{PbBr}_{0.33}\text{I}_{2.67}$  PNP along  $\overline{[201]}$  zone axis, scale bars 2 nm. (inset) HRTEM of a single PNP, scale bars 200 nm. (f) The steady-state PL spectra and (g) TRPL analysis of PNPs with and without an electron quencher (neat PNPs (PNPs@PAM), black, PNPs@PAM/Spiro-OMeTAD, red, and PNPs@ $\text{NiO}_x$ @PAM/Spiro-OMeTAD, blue).

aluminum (Al) foil with high periodicity.  $\text{NiO}_x$  is deposited in PAM via atomic layer deposition (ALD). Afterward,  $\text{NiO}_x$ -coated PAM ( $\text{NiO}_x$ @PAM) is transferred to  $\text{SnO}_2$ -covered ITO-PET ( $\text{SnO}_2$ @ITO-PET) by the Langmuir–Blodgett technique. Next, PNPs are grown inside the pore of  $\text{NiO}_x$ @PAM via the capillary-effect-assisted solution method, followed by the spin-coated deposition of spiro-OMeTAD. Finally, a top electrode of Au is evaporated. Photographs of  $\text{NiO}_x$ @PAM implemented on the  $\text{SnO}_2$ @ITO-PET, the complete device is shown in Figure 1d,e, respectively. The fabrication details can be found in the Experimental Section.

Figure 2a1,a2 is the PAM top view and cross-sectional scanning electron microscopy (SEM) image, respectively. The pitch of the PAM is 500 nm, the pore size is 300 nm, and the thickness is 500 nm. The chemically and mechanically robust PAM is an ideal nanoengineering template to guide PNPs' growth.<sup>5,54,55</sup> Besides, the geometry of PAM can be modulated by controlling the fabrication conditions. This allows one to explore the impact of diverse nanogeometry on the perform-

ance of cells. Figure 2b1,b2 demonstrates the conformal coating of  $\text{NiO}_x$  both on the top and in the nanochannels of the PAM. The tilted-angle views of PNPs encapsulated in  $\text{NiO}_x$ @PAM (PNPs@ $\text{NiO}_x$ @PAM) are shown in Figure 2c1,c2. Close contact is formed at the interfaces between PNPs and  $\text{NiO}_x/\text{SnO}_2$ , where photogenerated excitons are dissociated into free charges. This is a prerequisite for an efficient device, as the inferior contact at the interface is one of the leading causes of impeding charge collection efficiency. Figure 2c2 shows smooth surfaces of PNPs with no observable grain boundary, suggesting a high crystalline quality of PNPs. The cross-sectional SEM of the complete device is shown in Figure 2d. The low-magnification SEM Figure 2c1 & Figure S2 present the successful fabrication of high-density PNPs arrays with a large-scale uniformity and close to 100% pore-filling ratio, which is beneficial to avoid the formation of a shunting path.

To characterize a crystal lattice, a single  $\text{Cs}_{0.05}\text{FA}_{0.83}\text{MA}_{0.12}\text{PbBr}_{0.33}\text{I}_{2.67}$  PNP (inset of Figure 2e) with

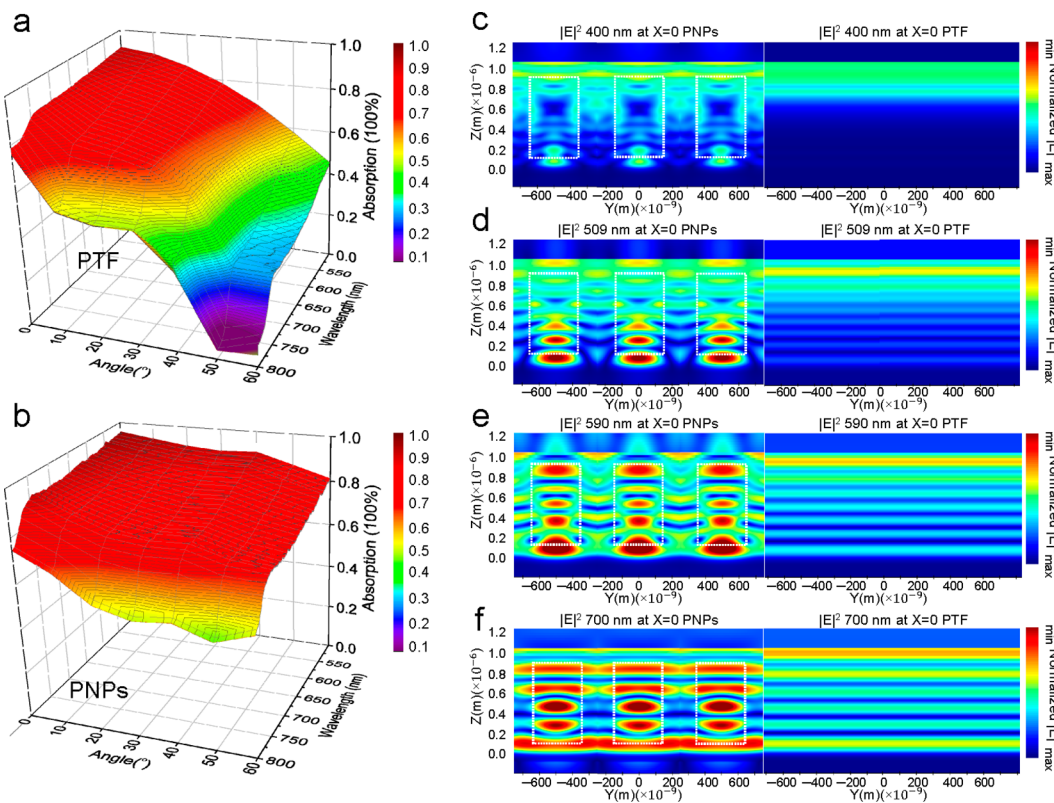


**Figure 3.** Light trapping enhanced absorption of PNP-based device. The UV-vis spectrum of (a) PTF and (b) PNP<sub>x</sub>@NiO<sub>x</sub>@PAM (PNPs) under different incident angles (from 0° to 60°). The absorption is recorded every 10°. Simulated cross-sectional electric field intensity distribution ( $|E|^2$ ) (normalized as min to max) in solar cells based on PNP<sub>x</sub>@PAM and PTF at input light (c)  $\lambda = 400$  nm, (d)  $\lambda = 509$  nm, (e)  $\lambda = 590$  nm, and (f)  $\lambda = 700$  nm. The details of Finite-Difference Time-Domain (FDTD) simulations can be found in the Experimental Section.

less than 100 nm diameter was used for high-resolution transmission electron microscopy (HRTEM) imaging. The HRTEM view along [201] zone axis Figure 2e shows clear lattice fringes with a spacing of 4.4 Å for the (112) planes. The fast Fourier transform analysis Figure S3 exhibits diffraction spots of [201] zone axis in a hexagonal symmetry.<sup>56</sup> Figure S4 shows X-ray diffraction (XRD) patterns of as-grown PNPs. All the XRD patterns match well with the cubic phase perovskites (space-group: *Pmm*,  $\alpha = 90^\circ$ , cell constant:  $a = 6.2874$  Å). No impurity diffraction peak is observed.

Photoluminescence (PL) and time-resolved photoluminescence (TRPL) spectra of PNPs have been acquired to understand the carrier dynamics. The PL spectra are obtained with 514 nm light excitation. Figure 2f plots three PL spectra from different material configurations, namely, PNPs@PAM (bare PNPs encapsulated in PAM), PNPs@PAM/Spiro-OMeTAD (spiro-OMeTAD layer atop the PNPs@PAM), and PNPs@NiO<sub>x</sub>@PAM/Spiro-OMeTAD (spiro-OMeTAD layer atop the PNPs@NiO<sub>x</sub>@PAM, the cross-sectional SEM is shown in Figure S5). The PNPs@PAM demonstrates a sharp PL peak at 780 nm. The introduction of spiro-OMeTAD significantly quenches the PL intensity, further reduced by the presence of NiO<sub>x</sub>, which is a good indication of efficient hole transfer in the PNPs@NiO<sub>x</sub>@PAM/Spiro-OMeTAD film.

The TRPL curves in Figure 2g also reveal the radial built-in electric field promotes charge collection. The decay curves are fitted with a biexponential model. Figure 2g retrieves a carrier lifetime of  $\tau_e = 76.30$  ns for PNPs@PAM.<sup>47,57</sup> Notably, the carrier lifetime of PNPs is of the same magnitude as the perovskite thin film (PTF) (Figure S6).<sup>58</sup> The long carrier

lifetime indicates a slow recombination rate, which allows photogenerated carriers to move in the PNP without constantly encountering traps. The other two material structures show pronounced PL quenching, with carrier lifetime reduced to  $\tau_e = 5.57$  ns by spiro-OMeTAD and further shortened to  $\tau_e = 1.17$  ns after the NiO<sub>x</sub> modification. The severer PL quenching yield of the NiO<sub>x</sub>-modified devices suggests the improved hole separation capability from PNPs to spiro-OMeTAD via the orthogonal carrier collection. In Figure S7, the full width at half-maximum of instrument response function (IRF) of 121 ps is estimated to confirm the accuracy.

Figure 3a,b plots the ultraviolet-visible (UV-vis) spectra of PTF and PNPs under different incident angles (from 0° to 60°). The PNPs possess an appealing capability of collecting photons over a broader range of incidence angles and wavelengths.<sup>59,60</sup> The enhanced absorption is more noticeable at high incidence angles.<sup>28,61</sup> Under the incident angle of 60°, 75.10% of absorption is achieved for PNPs at the wavelength of 700 nm; in contrast, that of PTF is only 30.52%.<sup>6,14,17,28,27</sup> The angular absorption advantage of PNPs is further demonstrated in simulated absorption Figure S8a and electric field intensity distribution ( $|E|^2$ ) Figure S9.<sup>20</sup> Additionally, Figure S8b measures the normalized values of  $J_{sc}$  as a function of incident light angle; the  $J_{sc}$  of PNP-based device retains 74.05% of its initial value at the incident angle of 60°, while that of PTF is merely 37.87%.<sup>29</sup>

To numerically study the optical absorption at different wavelengths in and outside PNPs, Figure 3c–f shows the simulated cross-sectional  $|E|^2$  of solar cells based on PNPs and PTF at input wavelengths of  $\lambda = 400$  nm,  $\lambda = 509$  nm,  $\lambda = 590$

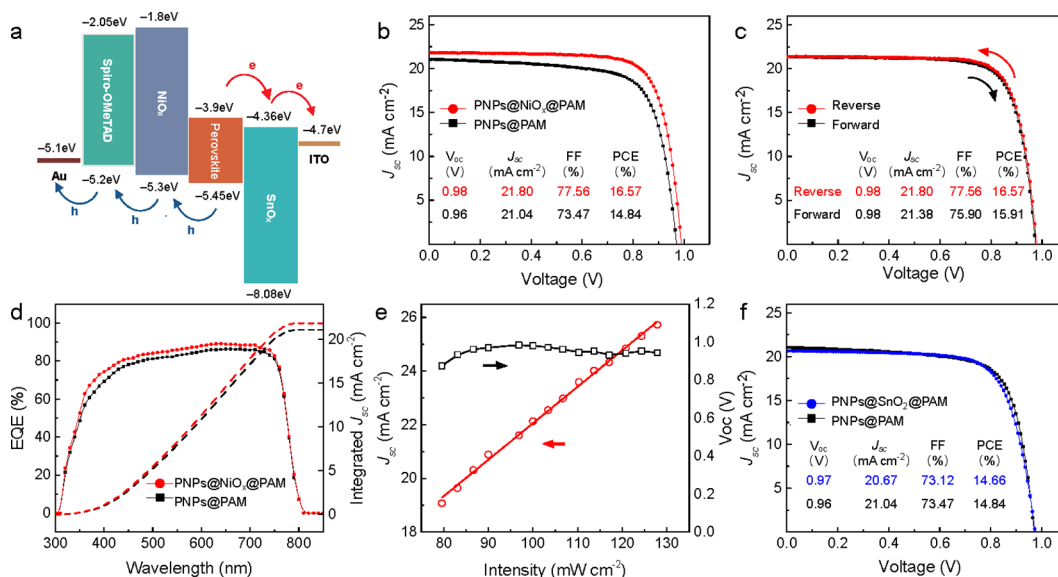


**Figure 4. Photovoltaic performance of PNP-based device.** (a) Energy-band diagram and (b) current density–voltage ( $J$ – $V$ ) characteristics of the champion devices based on PNP<sub>x</sub>@NiO<sub>x</sub>@PAM, red dot, and PNP<sub>x</sub>@PAM, black square, measured under standard AM1.5 solar radiation. (c)  $J$ – $V$  curves of the PNP<sub>x</sub>@NiO<sub>x</sub>@PAM-based best-performing device, recorded in reverse and forward scanning directions. (d) Solid lines are the external quantum efficiency (EQE) spectra of the best cells fabricated by PNP<sub>x</sub>@NiO<sub>x</sub>@PAM, red dot, and PNP<sub>x</sub>@PAM, black square. Dashed lines show short-circuit current density ( $J_{sc}$ ) integrated from the overlap integral of the EQE spectra with the standard AM1.5 solar emission. (e) The dependence of  $J_{sc}$ , red circle, and open-circuit voltage ( $V_{oc}$ ), black square, under different illumination intensities of the PNP<sub>x</sub>@NiO<sub>x</sub>@PAM-based device. (f)  $J$ – $V$  characteristics of best-performing PSCs based on PNP<sub>x</sub>@SnO<sub>2</sub>@PAM, blue dot, and PNP<sub>x</sub>@PAM, black square. (inset) Photovoltaic metrics derived from the  $J$ – $V$  curves. SnO<sub>2</sub>-coated PAM was prepared by ALD (see Experimental Section).

nm, and  $\lambda = 700$  nm. All the figures have the same color bar to make a fair comparison of  $|E|^2$ . Figure 3c–f witnessed long absorption paths along the length of PNPs, leading to a noticeable increase in absorption and distinct light-guiding behavior.<sup>62–66</sup> The light-coupling effect is further confirmed by the simulated top-view  $|E|^2$  in Figure S9a. Figure 3c shows the top zone dominates the absorption of short wavelengths. Benefiting from the nanoengineered periodic geometry, the benefit from the intensity of the standing wave in the PNPs at the longer wavelength (Figure 3d–f) appears to be more outstanding than at the short wavelength (Figure 3c).

To shed light on the impact of orthogonal carrier collection, the device based on PNP<sub>x</sub>@NiO<sub>x</sub>@PAM and PNP<sub>x</sub>@PAM are fabricated, with the energy-band diagram of the complete device and the current density–voltage ( $J$ – $V$ ) characteristics as shown in Figure 4a,b, respectively. In Figure 4a, band energy levels of SnO<sub>2</sub>,<sup>67</sup> spiro-OMeTAD,<sup>68</sup> NiO<sub>x</sub>,<sup>69</sup> and perovskite<sup>43</sup> are obtained from previously published literature. Perovskite shows a proper energy-level alignment with SnO<sub>2</sub>, NiO<sub>x</sub>, and spiro-MeOTAD. As shown in Figure 4b, the PNP<sub>x</sub>@PAM-based device has the best power conversion efficiency (PCE) of 14.84%,  $J_{sc}$  of 21.04 mA cm<sup>-2</sup>,  $V_{oc}$  of 0.96 V, and fill factor (FF) of 73.47%. Notably, the NiO<sub>x</sub> modification substantially improved performance. The NiO<sub>x</sub>-modified champion device achieved a high PCE of 16.57%,  $J_{sc}$  of 21.80 mA cm<sup>-2</sup>,  $V_{oc}$  of 0.98 V, and FF of 77.56%. Different  $J$ – $V$  scan directions were performed in Figure 4c to evaluate the hysteresis behavior of PNP<sub>x</sub>@NiO<sub>x</sub>@PAM-based devices. The difference in PCE between the forward and reverse scans is below 4% of absolute values, which reflects negligible hysteresis.<sup>37,56</sup> In general, hysteresis is associated with electric polarization, trapping and detrapping, and ion migration in perovskites. The negligible hysteresis in the PNP-based device is a consequence of the reduced overall defect density due to the high crystallinity of

PNPs, suppressed internal ion migration in PNPs by the PAM scaffold,<sup>70</sup> and efficient charge collection in the radial built-in electric field.<sup>37</sup>

Figure 4d shows the EQE spectra of the above PSCs. The PNP<sub>x</sub>@PAM-based devices contribute a high EQE of 81.2%–86.2% for broadband wavelength ( $\lambda = 500$ –750 nm).<sup>15,20,25–27,71</sup> After the NiO<sub>x</sub> modification, a substantially improved EQE of 84.0%–89.18% is witnessed over the whole wavelength range.<sup>20,49</sup> As a result, the NiO<sub>x</sub> modified device obtained an integrated  $J_{sc}$  of 21.80 mA cm<sup>-2</sup> from the EQE spectrum. Figure 4e demonstrates a near-linear dependency of  $J_{sc}$  on illumination intensity, which implies low nonradiative recombination. But  $V_{oc}$  merely improved from 0.89 to 1 V. The variation of  $V_{oc}$  can be attributed to thermal heating during the measurement, as a cooling chuck is not used.<sup>11</sup>

These results suggest that photogenerated holes from PNPs are efficiently transferred out by NiO<sub>x</sub>. Still, the exploration of ETL as a shell layer for electron conduct is necessary. Figure 4f measures the  $J$ – $V$  characteristics of PSCs with the device configuration of ITO-PET/SnO<sub>2</sub>/PNP<sub>x</sub>@SnO<sub>2</sub>@PAM/Spiro-OMeTAD/Au, and its SEM is shown in Figure S1. However, there is no detectable performance enhancement induced by the SnO<sub>2</sub> modification. This is primarily because the photogenerated holes along the PNPs crystal surface are much higher than in the crystal.<sup>49,50</sup> The  $J$ – $V$  curves of PNP-based PSCs with varying heights are provided in Figure S10. Performance improvement is witnessed up to an optimum PNP height of 500 nm owing to enhanced light absorption. A subsequent drop in the performance is observed with the PNP height around 1000 nm, attributed to the engendered charge recombination. To further improve PCE, Figure S11 studied the impact of NiO<sub>x</sub> thicknesses on the device performance. The PCE experienced an enhancement to an optimum NiO<sub>x</sub> thickness of 20 nm. A very thin NiO<sub>x</sub> layer undermines carrier

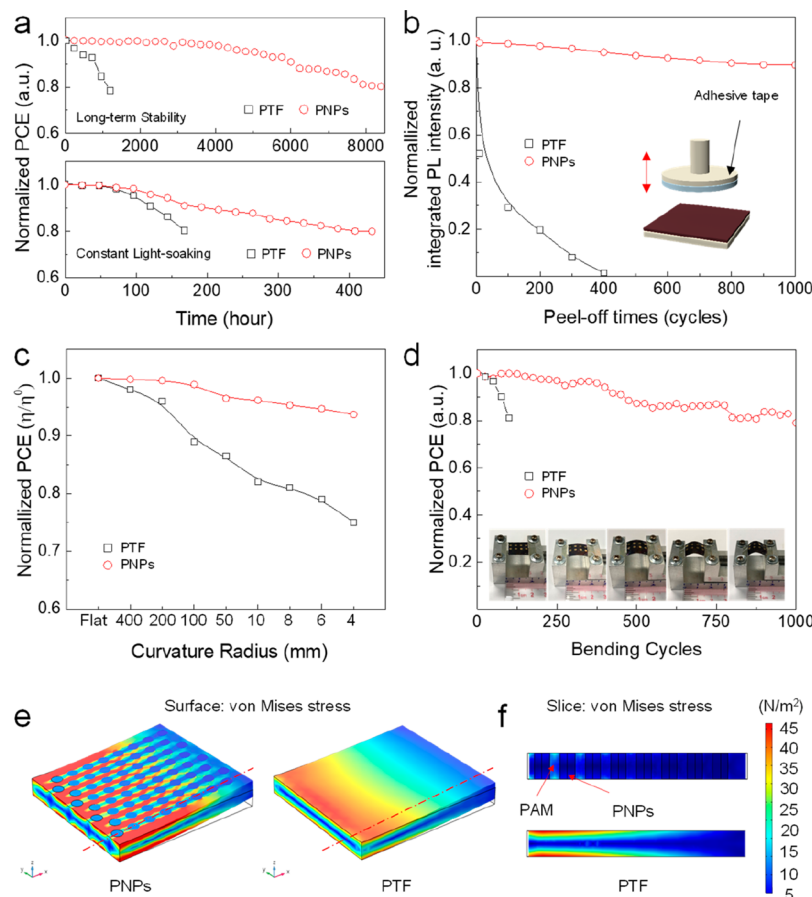


**Figure 5. Robust long-term stability, photostability, and flexibility of PNP-based devices.** (a) The long-term stability for unpackaged PNP<sub>x</sub>@NiO<sub>x</sub>@PAM-based (PNP-based), red dot, and PTF-based devices, black square, stored in a desiccator with a humidity of 10%–20%. The photostability tests under constant AM1.5G illumination for encapsulated PNP- and PTF-based devices. The performance was recorded every 24 h. (b) Normalized integrated PL intensity evolution of PTF and PNP-based devices over tape-assisted peel-off test cycles. (inset) Schematic of the test setup. (c) Normalized PCE of PNP- and PTF-based devices after bending within a specified radius from 400 to 4 mm. (d) Normalized PCE of PNP- and PTF-based devices as a function of bending cycles. The bending angle is fixed at around 120°. (inset) A picture of the setup for bending the flexible modules. (e) Surface stress mapping results for the 3D model figure of PNP<sub>x</sub>@NiO<sub>x</sub>@PAM and PTF. (f) The sliced stress distribution is extracted along the red dotted line in (e).

collection, while a too-thick NiO<sub>x</sub> layer adversely impacts efficiency.

The stability of perovskites is always the foremost concern, as they will rapidly degrade when exposed to oxygen, moisture, heat, and ultraviolet radiation.<sup>37</sup> Figure 5a performs the long-term stability test of the PNP- and PTF-based device by storing the unpackaged device in a desiccator (humidity 10%–20%). The PTF-based device rapidly dropped to 80% of the initial PCE after 960 h ( $T_{80} = 960$  h). By comparison, the PAM scaffold minimal moisture/oxygen infiltration and their lateral diffusion across the whole device led to a significantly boosted lifetime for PNP-based devices ( $T_{80} = 8400$  h).<sup>5,54,55</sup> Figure 5a also reveals the impact of light soaking on the photovoltaic performance. The encapsulated devices were exposed to continuous AM1.5G illumination in the ambient condition at 40 °C. The PTF quickly decayed to ~80% of the initial value after 168 h. In contrast, benefiting from the suppressed internal ion diffusion by PAM,<sup>70</sup> PNP-based devices experienced a considerable enhancement in photostability, which retained ~80% of original PCE after 408 h of light exposure. The weak adherence between the perovskite and substrates is one of the leading causes of poor mechanical stability. Figure 5b executes an adhesive tape-assisted peel-off process to examine the

adhesion between PNP<sub>x</sub> and substrates by evaluating integrated PL intensity decay. The PL of PTF almost diminished after 300 peel-off cycles due to the material delamination. Our PNP<sub>x</sub> are grown in PAM nanochannels (Figure S12); hence, they demonstrated strong adhesion, as no noticeable PL intensity decreased after 1000 cycles.

From the viewpoint of flexible devices, durability under bending stress is pivotal for applications such as wearable power supplies. Systematic bending tests, including curvature radius and cycles, were performed to ascertain mechanical stability. Figure 5c monitors the normalized PCE of PTF- and PNP-based devices versus the different curvature radii ( $R = \infty, 400, 200, 100, 50, 10, 8, 6, 4$  mm) in one bending cycle. The PCE was calculated from the device projection area. PTF- and PNP-based devices both witnessed negligible PCE degradation at the radius above 200 mm. Further decreasing the radius to 4 mm, the PNP-based device experienced a drop of 6.3% PCE. In contrast, the PTF reference exhibited a 25.0% PCE loss. Figure 5d further evaluates the change of normalized PCE of PTF- and PNP-based devices under repetitive bending. The PTF-based device showed an obviously deteriorated trend of PCE after 100 bending cycles. Indeed, PNP<sub>x</sub> manifested a much higher tolerance to fracture or deformation in multiple

bending cycles than the PTF counterpart, with 80% of the initial PCE retained after 1000 cycles. The SEM of PNPs and PTF under repetitive bending is shown in Figure S13. The strain and stress during bending induce cracks in PTF, which aggravates performance degradation.<sup>6,72,73</sup> In contrast, PNPs survive such large bending-induced stress.<sup>6,72,73</sup> Such excellent mechanical stability guarantees a steady output during continuous bending.<sup>74</sup> Still, a performance decay for the PNP-based device was observed after 1000 cycles, which can be caused by the deterioration of ITO-PET.<sup>75–77</sup> To further improve the mechanical durability, explorations about superior conductive and flexible materials need to be exerted, such as graphene materials, two-dimensional (2D) conductive material, etc.<sup>78–80</sup>

To visualize the stress distribution inside the device structure, a COMSOL simulation is performed in Figure 5e. Each PNP is individually encapsulated in the robust mechanical PAM.<sup>81</sup> Figure 5f extracts the cross-sectional stress distribution along the red dotted line in Figure 5e; its original data is plotted in Figure S14. Indeed, the nanoscale geometry is beneficial for facilitating the release of stress and tension, as almost all the compressive or tensile stress is concentrated in the PAM. This makes the stress most significant at the deformation point of PNPs as low as  $5.93\text{--}6.57\text{ N m}^{-2}$ , whereas that of PTF reaches  $42.54\text{--}43.41\text{ N m}^{-2}$ .

In summary, this work constructs crystalline and periodic 3D PNP arrays for efficient, flexible photovoltaics. Assemblies of PNPs, along with radial junctions, enable the realization of a highly flexible device with unique optoelectronic properties. Another appealing feature is the self-encapsulation of PAM, leading to robust long-term stability and photostability. Impressively, device nanostructure design can also facilitate strain relaxation. All these merits combined suggest that a PNP solar cell device structure is highly promising to achieve high device performance, especially for applications that require flexibility, if further material optimization can be conducted in the future.

## ASSOCIATED CONTENT

### Supporting Information

The Supporting Information is available free of charge at <https://pubs.acs.org/doi/10.1021/acs.nanolett.2c03694>.

Materials, free-standing PAM preparation, ALD depositions of  $\text{NiO}_x$  and  $\text{SnO}_2$ , COMSOL Multiphysics stress distribution analysis ([DOCX](#))

## AUTHOR INFORMATION

### Corresponding Author

Zhiyong Fan – Department of Electronic and Computer Engineering and Guangdong-Hong Kong-Macao Joint Laboratory for Intelligent Micro-Nano Optoelectronic Technology, The Hong Kong University of Science and Technology, Kowloon 999077 Hong Kong, China; Shenzhen Research Institute, The Hong Kong University of Science and Technology, Shenzhen 518057, China; [orcid.org/0000-0002-5397-0129](#); Email: [eezfan@ust.hk](mailto:eezfan@ust.hk)

### Authors

Yiyi Zhu – Department of Electronic and Computer Engineering, The Hong Kong University of Science and Technology, Kowloon 999077 Hong Kong, China; Shenzhen

Research Institute, The Hong Kong University of Science and Technology, Shenzhen 518057, China

Lei Shu – Department of Electronic and Computer Engineering, The Hong Kong University of Science and Technology, Kowloon 999077 Hong Kong, China; Shenzhen Research Institute, The Hong Kong University of Science and Technology, Shenzhen 518057, China

Swapna Deep Poddar – Department of Electronic and Computer Engineering, The Hong Kong University of Science and Technology, Kowloon 999077 Hong Kong, China; Shenzhen Research Institute, The Hong Kong University of Science and Technology, Shenzhen 518057, China

Qianpeng Zhang – Department of Electronic and Computer Engineering, The Hong Kong University of Science and Technology, Kowloon 999077 Hong Kong, China; Shenzhen Research Institute, The Hong Kong University of Science and Technology, Shenzhen 518057, China

Zhesi Chen – Department of Electronic and Computer Engineering, The Hong Kong University of Science and Technology, Kowloon 999077 Hong Kong, China; Shenzhen Research Institute, The Hong Kong University of Science and Technology, Shenzhen 518057, China

Yucheng Ding – Department of Electronic and Computer Engineering, The Hong Kong University of Science and Technology, Kowloon 999077 Hong Kong, China; Shenzhen Research Institute, The Hong Kong University of Science and Technology, Shenzhen 518057, China

Zhenghao Long – Department of Electronic and Computer Engineering, The Hong Kong University of Science and Technology, Kowloon 999077 Hong Kong, China; Shenzhen Research Institute, The Hong Kong University of Science and Technology, Shenzhen 518057, China

Suman Ma – Department of Electronic and Computer Engineering, The Hong Kong University of Science and Technology, Kowloon 999077 Hong Kong, China; Department of Materials Science and Engineering, Shenzhen, Southern University of Science and Technology, Shenzhen 518055, China

Beitao Ren – Department of Electronic and Computer Engineering, The Hong Kong University of Science and Technology, Kowloon 999077 Hong Kong, China; Shenzhen Research Institute, The Hong Kong University of Science and Technology, Shenzhen 518057, China

Xiao Qiu – Department of Electronic and Computer Engineering, The Hong Kong University of Science and Technology, Kowloon 999077 Hong Kong, China; Shenzhen Research Institute, The Hong Kong University of Science and Technology, Shenzhen 518057, China

Complete contact information is available at:  
<https://pubs.acs.org/10.1021/acs.nanolett.2c03694>

### Notes

The authors declare no competing financial interest.

## ACKNOWLEDGMENTS

This work is supported by the General Research Fund (Project Nos. 16205321, 16214619) from the Hong Kong Research Grant Council, the Science and Technology Plan of Shenzhen (Project Nos. JCYJ20170818114107730, JCYJ2018030617492335), Guangdong-Hong Kong-Macao Intelligent Micro-Nano Optoelectronic Technology Joint Laboratory (Project No. 2020B1212030010). The authors

also acknowledge the support from the Center for 1D/2D Quantum Materials and the State Key Laboratory of Advanced Displays and Optoelectronics Technologies at HKUST, and the Foshan Innovative and Entrepreneurial Research Team Program (2018IT100031).

## ■ REFERENCES

- (1) Zhou, Y.; Yang, S.; Yin, X.; Han, J.; Tai, M.; Zhao, X.; Chen, H.; Gu, Y.; Wang, N.; Lin, H. Enhancing electron transport via graphene quantum dot/SnO<sub>2</sub> composites for efficient and durable flexible perovskite photovoltaics. *Journal of Materials Chemistry A* **2019**, *7* (4), 1878–1888.
- (2) Zhou, Y.; Li, X.; Lin, H. To be higher and stronger—metal oxide electron transport materials for perovskite solar cells. *Small* **2020**, *16* (15), 1902579.
- (3) Yang, B.; Xiong, Y.; Ma, K.; Liu, S.; Tao, X. Recent advances in wearable textile-based triboelectric generator systems for energy harvesting from human motion. *EcoMater.* **2020**, *2* (4), e12054.
- (4) Roldán-Carmona, C.; Malinkiewicz, O.; Soriano, A.; Minguez Espallargas, G.; García, A.; Reinecke, P.; Kroyer, T.; Dar, M. I.; Nazeeruddin, M. K.; Bolink, H. J. Flexible high efficiency perovskite solar cells. *Energy Environ. Sci.* **2014**, *7* (3), 994–997.
- (5) Gu, L.; Zhang, D.; Kam, M.; Zhang, Q.; Poddar, S.; Fu, Y.; Mo, X.; Fan, Z. Significantly improved black phase stability of FAPbI<sub>3</sub> nanowires via spatially confined vapor phase growth in nanoporous templates. *Nanoscale* **2018**, *10* (32), 15164–15172.
- (6) Zhang, Q.; Zhang, D.; Gu, L.; Tsui, K.-H.; Poddar, S.; Fu, Y.; Shu, L.; Fan, Z. Three-Dimensional Perovskite Nanophotonic Wire Array-Based Light-Emitting Diodes with Significantly Improved Efficiency and Stability. *ACS Nano* **2020**, *14* (2), 1577–1585.
- (7) Leung, S.-F.; Gu, L.; Zhang, Q.; Tsui, K.-H.; Shieh, J.-M.; Shen, C.-H.; Hsiao, T.-H.; Hsu, C.-H.; Lu, L.; Li, D.; et al. Roll-to-roll fabrication of large scale and regular arrays of three-dimensional nanospikes for high efficiency and flexible photovoltaics. *Sci. Rep.* **2015**, *4* (1), 1–8.
- (8) Kong, H.; Sun, W.; Zhou, H. Progress in flexible perovskite solar cells with improved efficiency. *Journal of Semiconductors* **2021**, *42* (10), 101605.
- (9) Davis, M.; Yu, Z. A review of flexible halide perovskite solar cells towards scalable manufacturing and environmental sustainability. *Journal of Semiconductors* **2020**, *41* (4), 041603.
- (10) Fan, Z.; Ruebusch, D. J.; Rathore, A. A.; Kapadia, R.; Egen, O.; Leu, P. W.; Javey, A. Challenges and prospects of nanopillar-based solar cells. *Nano Research* **2009**, *2* (11), 829–843.
- (11) Fan, Z.; Razavi, H.; Do, J.-w.; Moriwaki, A.; Egen, O.; Chueh, Y.-L.; Leu, P. W.; Ho, J. C.; Takahashi, T.; Reichertz, L. A.; Neale, S.; Yu, K.; Wu, M.; Ager, J. W.; Javey, A.; et al. Three-dimensional nanopillar-array photovoltaics on low-cost and flexible substrates. *Nature materials* **2009**, *8* (8), 648–653.
- (12) Lewis, N. S. Toward cost-effective solar energy use. *Science* **2007**, *315* (5813), 798–801.
- (13) Garnett, E. C.; Brongersma, M. L.; Cui, Y.; McGehee, M. D. Nanowire solar cells. *Annu. Rev. Mater. Res.* **2011**, *41*, 269–295.
- (14) Yu, Z.; Raman, A.; Fan, S. Fundamental limit of nanophotonic light trapping in solar cells. *Proc. Natl. Acad. Sci. U. S. A.* **2010**, *107* (41), 17491–17496.
- (15) Kayes, B. M.; Atwater, H. A.; Lewis, N. S. Comparison of the device physics principles of planar and radial p–n junction nanorod solar cells. *Journal of applied physics* **2005**, *97* (11), 114302.
- (16) Zhang, Y.; Wang, L.-W.; Mascarenhas, A. “Quantum Coaxial Cables” for Solar Energy Harvesting. *Nano Lett.* **2007**, *7* (5), 1264–1269.
- (17) Li, Y.; Qian, F.; Xiang, J.; Lieber, C. M. Nanowire electronic and optoelectronic devices. *Mater. Today* **2006**, *9* (10), 18–27.
- (18) Brongersma, M. L.; Cui, Y.; Fan, S. Light management for photovoltaics using high-index nanostructures. *Nature materials* **2014**, *13* (5), 451–460.
- (19) Yip, S.; Shen, L.; Ho, J. C. Recent advances in flexible photodetectors based on 1D nanostructures. *Journal of Semiconductors* **2019**, *40* (11), 111602.
- (20) Kelzenberg, M. D.; Boettcher, S. W.; Petykiewicz, J. A.; Turner-Evans, D. B.; Putnam, M. C.; Warren, E. L.; Spurgeon, J. M.; Briggs, R. M.; Lewis, N. S.; Atwater, H. A. Enhanced absorption and carrier collection in Si wire arrays for photovoltaic applications. *Nature materials* **2010**, *9* (3), 239–244.
- (21) Elbersen, R.; Vrijelaar, W.; Tiggelaar, R. M.; Gardeniers, H.; Huskens, J. Fabrication and doping methods for silicon nano-and micropillar arrays for solar-cell applications: a review. *Advanced materials* **2015**, *27* (43), 6781–6796.
- (22) Huynh, W. U.; Dittmer, J. J.; Alivisatos, A. P. Hybrid nanorod-polymer solar cells. *Science* **2002**, *295* (5564), 2425–2427.
- (23) Yang, Y.; Mielczarek, K.; Aryal, M.; Zakhidov, A.; Hu, W. Nanoimprinted polymer solar cell. *ACS Nano* **2012**, *6* (4), 2877–2892.
- (24) Law, M.; Greene, L. E.; Johnson, J. C.; Saykally, R.; Yang, P. Nanowire dye-sensitized solar cells. *Nature materials* **2005**, *4* (6), 455–459.
- (25) Garnett, E.; Yang, P. Light trapping in silicon nanowire solar cells. *Nano Lett.* **2010**, *10* (3), 1082–1087.
- (26) Leung, S.-F.; Yu, M.; Lin, Q.; Kwon, K.; Ching, K.-L.; Gu, L.; Yu, K.; Fan, Z. Efficient photon capturing with ordered three-dimensional nanowell arrays. *Nano Lett.* **2012**, *12* (7), 3682–3689.
- (27) Tavakoli, M. M.; Tsui, K.-H.; Zhang, Q.; He, J.; Yao, Y.; Li, D.; Fan, Z. Highly efficient flexible perovskite solar cells with antireflection and self-cleaning nanostructures. *ACS Nano* **2015**, *9* (10), 10287–10295.
- (28) Hua, B.; Lin, Q.; Zhang, Q.; Fan, Z. Efficient photon management with nanostructures for photovoltaics. *Nanoscale* **2013**, *5* (15), 6627–6640.
- (29) Huang, H.; Lu, L.; Wang, J.; Yang, J.; Leung, S.-F.; Wang, Y.; Chen, D.; Chen, X.; Shen, G.; Li, D.; et al. Performance enhancement of thin-film amorphous silicon solar cells with low cost nanodent plasmonic substrates. *Energy Environ. Sci.* **2013**, *6* (10), 2965–2971.
- (30) Hua, B.; Wang, B.; Yu, M.; Leu, P. W.; Fan, Z. Rational geometrical design of multi-diameter nanopillars for efficient light harvesting. *Nano Energy* **2013**, *2* (5), 951–957.
- (31) Lin, Q.; Leung, S.-F.; Lu, L.; Chen, X.; Chen, Z.; Tang, H.; Su, W.; Li, D.; Fan, Z. Inverted nanocone-based thin film photovoltaics with omnidirectionally enhanced performance. *ACS Nano* **2014**, *8* (6), 6484–6490.
- (32) Lauhon, L. J.; Gudiksen, M. S.; Wang, D.; Lieber, C. M. Epitaxial core–shell and core–multishell nanowire heterostructures. *nature* **2002**, *420* (6911), 57–61.
- (33) Qian, F.; Li, Y.; Gradečák, S.; Wang, D.; Barrelet, C. J.; Lieber, C. M. Gallium nitride-based nanowire radial heterostructures for nanophotonics. *Nano Lett.* **2004**, *4* (10), 1975–1979.
- (34) Qian, F.; Li, Y.; Gradečák, S.; Park, H.-G.; Dong, Y.; Ding, Y.; Wang, Z. L.; Lieber, C. M. Multi-quantum-well nanowire heterostructures for wavelength-controlled lasers. *Nature materials* **2008**, *7* (9), 701–706.
- (35) Kalytchuk, S.; Gupta, S.; Zhovtiuk, O.; Vanek, A.; Kershaw, S. V.; Fu, H.; Fan, Z.; Kwok, E. C.; Wang, C.-F.; Teoh, W. Y.; et al. Semiconductor nanocrystals as luminescent down-shifting layers to enhance the efficiency of thin-film CdTe/CdS and crystalline Si solar cells. *J. Phys. Chem. C* **2014**, *118* (30), 16393–16400.
- (36) Wangperawong, A.; Bent, S. F. Three-dimensional nanojunction device models for photovoltaics. *Appl. Phys. Lett.* **2011**, *98* (23), 233106.
- (37) Zhu, Y.; Poddar, S.; Shu, L.; Fu, Y.; Fan, Z. Recent Progress on Interface Engineering for High-Performance, Stable Perovskites Solar Cells. *Advanced Materials Interfaces* **2020**, *7* (11), 2000118.
- (38) Qiu, L.; Deng, J.; Lu, X.; Yang, Z.; Peng, H. Integrating perovskite solar cells into a flexible fiber. *Angew. Chem., Int. Ed.* **2014**, *53* (39), 10425–10428.

- (39) Qiu, L.; He, S.; Yang, J.; Deng, J.; Peng, H. Fiber-shaped perovskite solar cells with high power conversion efficiency. *Small* **2016**, *12* (18), 2419–2424.
- (40) Xue, J.; Wang, R.; Yang, Y. The surface of halide perovskites from nano to bulk. *Nature Reviews Materials* **2020**, *5* (11), 809–827.
- (41) Zhang, Q.; Tavakoli, M. M.; Gu, L.; Zhang, D.; Tang, L.; Gao, Y.; Guo, J.; Lin, Y.; Leung, S.-F.; Poddar, S. Efficient metal halide perovskite light-emitting diodes with significantly improved light extraction on nanophotonic substrates. *Nat. Commun.* **2019**, *10* (1), 1–9.
- (42) Zhang, D.; Gu, L.; Zhang, Q.; Lin, Y.; Lien, D.-H.; Kam, M.; Poddar, S.; Garnett, E. C.; Javey, A.; Fan, Z. Increasing photoluminescence quantum yield by nanophotonic design of quantum-confined halide perovskite nanowire arrays. *Nano Lett.* **2019**, *19* (5), 2850–2857.
- (43) Gutsche, C.; Lysov, A.; Braam, D.; Regolin, I.; Keller, G.; Li, Z. A.; Geller, M.; Spasova, M.; Prost, W.; Tegude, F. J. n-GaAs/InGaP/p-GaAs Core-Multishell Nanowire Diodes for Efficient Light-to-Current Conversion. *Adv. Funct. Mater.* **2012**, *22* (5), 929–936.
- (44) Dong, Y.; Tian, B.; Kempa, T. J.; Lieber, C. M. Coaxial group III–nitride nanowire photovoltaics. *Nano Lett.* **2009**, *9* (5), 2183–2187.
- (45) Zhu, Y.; Shu, L.; Zhang, Q.; Zhu, Y.; Poddar, S.; Wang, C.; He, Z.; Fan, Z. Moth eye-inspired highly efficient, robust, and neutral-colored semitransparent perovskite solar cells for building-integrated photovoltaics. *EcoMater.* **2021**, *3* (4), e12117.
- (46) Zhu, Y.; Zhang, Q.; Kam, M.; Poddar, S.; Gu, L.; Liang, S.; Qi, P.; Miao, F.; Fan, Z. Vapor phase fabrication of three-dimensional arrayed BiI<sub>3</sub> nanosheets for cost-effective solar cells. *InfoMater.* **2020**, *2* (5), 975–983.
- (47) Stranks, S. D.; Eperon, G. E.; Grancini, G.; Menelaou, C.; Alcocer, M. J.; Leijtens, T.; Herz, L. M.; Petrozza, A.; Snaith, H. J. Electron-hole diffusion lengths exceeding 1 micrometer in an organometal trihalide perovskite absorber. *Science* **2013**, *342* (6156), 341–344.
- (48) Xing, G.; Mathews, N.; Sun, S.; Lim, S. S.; Lam, Y. M.; Grätzel, M.; Mhaisalkar, S.; Sum, T. C. Long-range balanced electron-and hole-transport lengths in organic-inorganic CH<sub>3</sub>NH<sub>3</sub>PbI<sub>3</sub>. *Science* **2013**, *342* (6156), 344–347.
- (49) You, P.; Tang, G.; Cao, J.; Shen, D.; Ng, T.-W.; Hawash, Z.; Wang, N.; Liu, C.-K.; Lu, W.; Tai, Q. 2D materials for conducting holes from grain boundaries in perovskite solar cells. *Light: Science & Applications* **2021**, *10* (1), 1–12.
- (50) Yun, J. S.; Ho-Baillie, A.; Huang, S.; Woo, S. H.; Heo, Y.; Seidel, J.; Huang, F.; Cheng, Y.-B.; Green, M. A. Benefit of grain boundaries in organic–inorganic halide planar perovskite solar cells. *Journal of physical chemistry letters* **2015**, *6* (5), 875–880.
- (51) Fu, Y.; Poddar, S.; Ren, B.; Xie, Y.; Zhang, Q.; Zhang, D.; Cao, B.; Tang, Y.; Ding, Y.; Qiu, X.; et al. Strongly Quantum-Confining Perovskite Nanowire Arrays for Color-Tunable Blue-Light-Emitting Diodes. *ACS Nano* **2022**, *16*, 8388–8398.
- (52) Jiang, J.; Wang, X.; Zhang, Q.; Li, J.; Zhang, X. Thermal oxidation of Ni films for p-type thin-film transistors. *Phys. Chem. Chem. Phys.* **2013**, *15* (18), 6875–6878.
- (53) Liu, A.; Liu, G.; Zhu, H.; Shin, B.; Fortunato, E.; Martins, R.; Shan, F. Hole mobility modulation of solution-processed nickel oxide thin-film transistor based on high-k dielectric. *Appl. Phys. Lett.* **2016**, *108* (23), 233506.
- (54) Waleed, A.; Tavakoli, M. M.; Gu, L.; Hussain, S.; Zhang, D.; Poddar, S.; Wang, Z.; Zhang, R.; Fan, Z. All inorganic cesium lead iodide perovskite nanowires with stabilized cubic phase at room temperature and nanowire array-based photodetectors. *Nano Lett.* **2017**, *17* (8), 4951–4957.
- (55) Waleed, A.; Tavakoli, M. M.; Gu, L.; Wang, Z.; Zhang, D.; Manikandan, A.; Zhang, Q.; Zhang, R.; Chueh, Y.-L.; Fan, Z. Lead-free perovskite nanowire array photodetectors with drastically improved stability in nanoengineering templates. *Nano Lett.* **2017**, *17* (1), 523–530.
- (56) Tsai, H.; Nie, W.; Lin, Y. H.; Blancon, J. C.; Tretiak, S.; Even, J.; Gupta, G.; Ajayan, P. M.; Mohite, A. D. Effect of precursor solution aging on the crystallinity and photovoltaic performance of perovskite solar cells. *Adv. Energy Mater.* **2017**, *7* (11), 1602159.
- (57) Di, J.; Chang, J.; Liu, S. Recent progress of two-dimensional lead halide perovskite single crystals: Crystal growth, physical properties, and device applications. *EcoMater.* **2020**, *2* (3), e12036.
- (58) Yoo, J. J.; Seo, G.; Chua, M. R.; Park, T. G.; Lu, Y.; Rotermund, F.; Kim, Y.-K.; Moon, C. S.; Jeon, N. J.; Correa-Baena, J.-P.; Bulović, V.; Shin, S. S.; Bawendi, M. G.; Seo, J. Efficient perovskite solar cells via improved carrier management. *Nature* **2021**, *590* (7847), 587–593.
- (59) Yu, R.; Lin, Q.; Leung, S.-F.; Fan, Z. Nanomaterials and nanostructures for efficient light absorption and photovoltaics. *Nano Energy* **2012**, *1* (1), 57–72.
- (60) Polman, A.; Atwater, H. A. Photonic design principles for ultrahigh-efficiency photovoltaics. *Nature materials* **2012**, *11* (3), 174–177.
- (61) Chueh, Y.-L.; Fan, Z.; Takei, K.; Ko, H.; Kapadia, R.; Rathore, A. A.; Miller, N.; Yu, K.; Wu, M.; Haller, E.; et al. Black Ge based on crystalline/amorphous core/shell nanoneedle arrays. *Nano Lett.* **2010**, *10* (2), 520–523.
- (62) Chen, J.; Fu, Y.; Samad, L.; Dang, L.; Zhao, Y.; Shen, S.; Guo, L.; Jin, S. Vapor-phase epitaxial growth of aligned nanowire networks of cesium lead halide perovskites (CsPbX<sub>3</sub>, X = Cl, Br, I). *Nano Lett.* **2017**, *17* (1), 460–466.
- (63) Oksenberg, E.; Sanders, E.; Popovitz-Biro, R.; Houben, L.; Joselevich, E. Surface-guided CsPbBr<sub>3</sub> perovskite nanowires on flat and faceted sapphire with size-dependent photoluminescence and fast photoconductive response. *Nano Lett.* **2018**, *18* (1), 424–433.
- (64) Shoaib, M.; Zhang, X.; Wang, X.; Zhou, H.; Xu, T.; Wang, X.; Hu, X.; Liu, H.; Fan, X.; Zheng, W.; et al. Directional growth of ultralong CsPbBr<sub>3</sub> perovskite nanowires for high-performance photodetectors. *J. Am. Chem. Soc.* **2017**, *139* (44), 15592–15595.
- (65) Oksenberg, E.; Fai, C.; Schebykin, I. G.; Joselevich, E.; Unger, E. L.; Unold, T.; Hages, C.; Merdasa, A. Deconvoluting Energy Transport Mechanisms in Metal Halide Perovskites Using CsPbBr<sub>3</sub> Nanowires as a Model System. *Adv. Funct. Mater.* **2021**, *31* (22), 2010704.
- (66) Shang, Q.; Li, C.; Zhang, S.; Liang, Y.; Liu, Z.; Liu, X.; Zhang, Q. Enhanced optical absorption and slowed light of reduced-dimensional CsPbBr<sub>3</sub> nanowire crystal by exciton–polariton. *Nano Lett.* **2020**, *20* (2), 1023–1032.
- (67) Kam, M.; Zhu, Y.; Zhang, D.; Gu, L.; Chen, J.; Fan, Z. Efficient Mixed-Cation Mixed-Halide Perovskite Solar Cells by All-Vacuum Sequential Deposition Using Metal Oxide Electron Transport Layer. *Solar RRL* **2019**, *3* (7), 1900050.
- (68) Bi, D.; Tress, W.; Dar, M. I.; Gao, P.; Luo, J.; Renevier, C.; Schenk, K.; Abate, A.; Giordano, F.; Baena, J.-P. C.; et al. Efficient luminescent solar cells based on tailored mixed-cation perovskites. *Sci. Adv.* **2016**, *2* (1), e1501170.
- (69) Chen, W.; Liu, F. Z.; Feng, X. Y.; Djurišić, A. B.; Chan, W. K.; He, Z. B. Cesium doped NiO<sub>x</sub> as an efficient hole extraction layer for inverted planar perovskite solar cells. *Adv. Energy Mater.* **2017**, *7* (19), 1700722.
- (70) Kwon, H. C.; Kim, A.; Lee, H.; Lee, D.; Jeong, S.; Moon, J. Parallelized nanopillar perovskites for semitransparent solar cells using an anodized aluminum oxide scaffold. *Adv. Energy Mater.* **2016**, *6* (20), 1601055.
- (71) Law, M.; Goldberger, J.; Yang, P. Semiconductor nanowires and nanotubes. *Annu. Rev. Mater. Res.* **2004**, *34* (1), 83–122.
- (72) Zhang, C.; Song, Y.; Wang, M.; Yin, M.; Zhu, X.; Tian, L.; Wang, H.; Chen, X.; Fan, Z.; Lu, L.; et al. Efficient and flexible thin film amorphous silicon solar cells on nanotextured polymer substrate using sol–gel based nanoimprinting method. *Adv. Funct. Mater.* **2017**, *27* (13), 1604720.
- (73) Jiang, C.; Sun, X.; Tan, K.; Lo, G.; Kyaw, A.; Kwong, D. High-bendability flexible dye-sensitized solar cell with a nanoparticle-

- modified ZnO-nanowire electrode. *Appl. Phys. Lett.* **2008**, *92* (14), 143101.
- (74) Lin, Q.; Huang, H.; Jing, Y.; Fu, H.; Chang, P.; Li, D.; Yao, Y.; Fan, Z. Flexible photovoltaic technologies. *Journal of Materials Chemistry C* **2014**, *2* (7), 1233–1247.
- (75) Zhang, Y.; Wu, Z.; Li, P.; Ono, L. K.; Qi, Y.; Zhou, J.; Shen, H.; Surya, C.; Zheng, Z. Fully solution-processed TCO-free semi-transparent perovskite solar cells for tandem and flexible applications. *Adv. Energy Mater.* **2018**, *8* (1), 1701569.
- (76) Kim, J.-H.; Seok, H.-J.; Seo, H.-J.; Seong, T.-Y.; Heo, J. H.; Lim, S.-H.; Ahn, K.-J.; Kim, H.-K. Flexible ITO films with atomically flat surfaces for high performance flexible perovskite solar cells. *Nanoscale* **2018**, *10* (44), 20587–20598.
- (77) Lewis, J. Material challenge for flexible organic devices. *Mater. Today* **2006**, *9* (4), 38–45.
- (78) Kim, B. J.; Kim, D. H.; Lee, Y.-Y.; Shin, H.-W.; Han, G. S.; Hong, J. S.; Mahmood, K.; Ahn, T. K.; Joo, Y.-C.; Hong, K. S.; et al. Highly efficient and bending durable perovskite solar cells: toward a wearable power source. *Energy Environ. Sci.* **2015**, *8* (3), 916–921.
- (79) Li, Y.; Meng, L.; Yang, Y. M.; Xu, G.; Hong, Z.; Chen, Q.; You, J.; Li, G.; Yang, Y.; Li, Y. High-efficiency robust perovskite solar cells on ultrathin flexible substrates. *Nat. Commun.* **2016**, *7* (1), 1–10.
- (80) Luo, Q.; Ma, H.; Hou, Q.; Li, Y.; Ren, J.; Dai, X.; Yao, Z.; Zhou, Y.; Xiang, L.; Du, H.; He, H.; Wang, N.; Jiang, K.; Lin, H.; Zhang, H.; Guo, Z. All-Carbon-Electrode-Based Endurable Flexible Perovskite Solar Cells. *Adv. Funct. Mater.* **2018**, *28* (11), 1706777.
- (81) Ko, S.; Lee, D.; Jee, S.; Park, H.; Lee, K.; Hwang, W. Mechanical properties and residual stress in porous anodic alumina structures. *Thin solid films* **2006**, *515* (4), 1932–1937.

## □ Recommended by ACS

### Laser Irradiation Effect on the p-GaSe/n-HfS<sub>2</sub> PN-Heterojunction for High-Performance Phototransistors

Zahir Muhammad, Weisheng Zhao, et al.

JULY 22, 2022

ACS APPLIED MATERIALS & INTERFACES

READ ▶

### High-Luminance Microsized CH<sub>3</sub>NH<sub>3</sub>PbBr<sub>3</sub> Single-Crystal-Based Light-Emitting Diodes via a Facile Liquid-Insulator Bridging Route

Huanyang Zhang, Jiansheng Jie, et al.

APRIL 11, 2022

ACS NANO

READ ▶

### Toward an Ultrahigh-Performance Near-Infrared Photoresponsive Field-Effect Transistor Using a Lead Phthalocyanine/MoS<sub>2</sub> Organic-Inorganic Planar Heteroj...

Sunan Xu, Yingquan Peng, et al.

JUNE 07, 2022

ACS APPLIED ELECTRONIC MATERIALS

READ ▶

### High-Performance Broadband Photodetectors Based on n-MoS<sub>2</sub>/p-Ge<sub>0.9</sub>Sn<sub>0.1</sub> Heterojunctions

Kaixiang Shu, Jingbo Li, et al.

JULY 16, 2021

ACS APPLIED ELECTRONIC MATERIALS

READ ▶

Get More Suggestions >